Science Advances
AAAS

advances.sciencemag.org/cgi/content/full/6/5/eaaw8065/DC1

Supplementary Materials for

Near-infrared and visible light dual-mode organic photodetectors

Zhaojue Lan, Yanlian Lei, Wing Kin Edward Chan, Shuming Chen, Dan Luo*, Furong Zhu*

*Corresponding author. Email: luod@sustc.edu.cn (D.L.); frzhu@hkbu.edu.hk (F.Z.)

Published 31 January 2020, *Sci. Adv.* **6**, eaaw8065 (2020)
DOI: 10.1126/sciadv.aaw8065

This PDF file includes:

1. *OPD with a ternary single active layer*

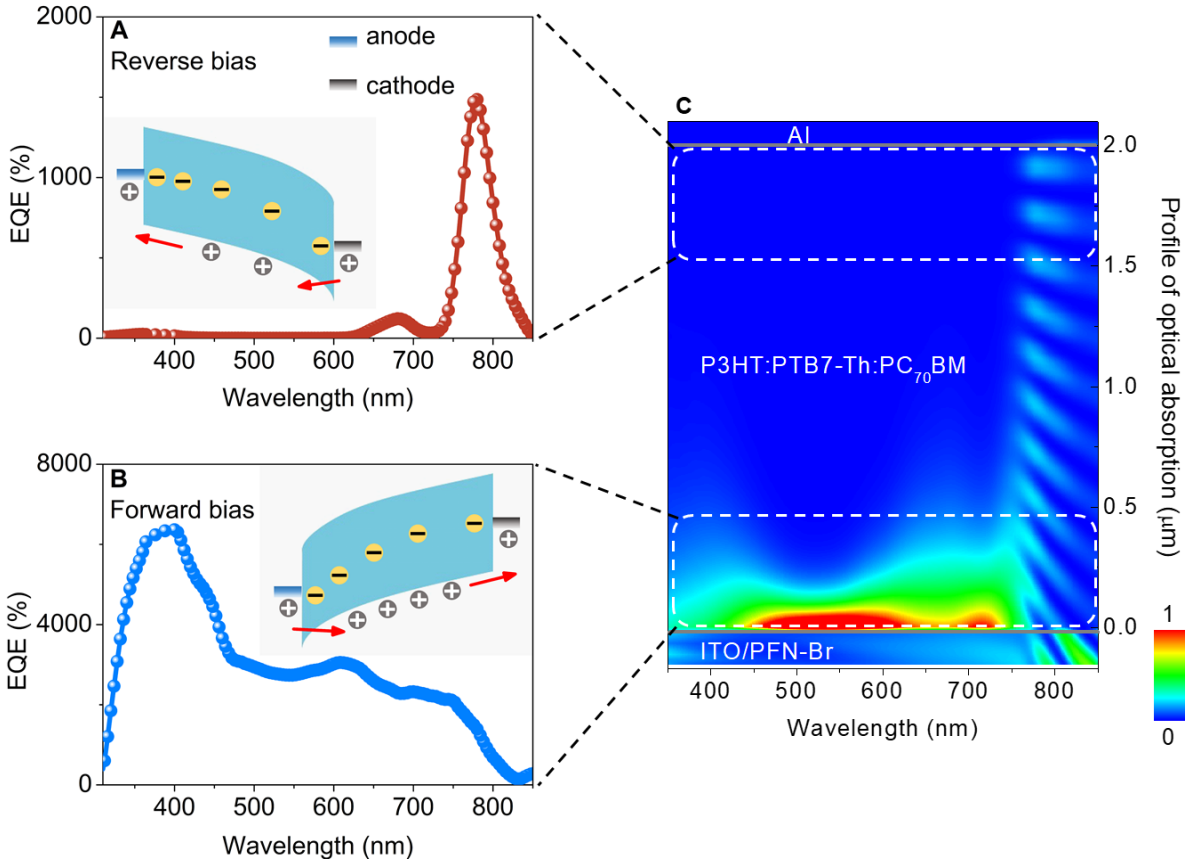

Fig. S1. Bias polarity–dependent spectral responses of a P3HT:PTB7-Th:$PC_{70}BM$ (70:30:1)–based PM OPD. EQE spectra measured for the PM OPD at (**A**) a reverse bias of -50 V and (**B**) a forward bias of 50 V, (**C**) distribution of photo-generated electrons in a 2000 nm thick P3HT:PTB7-Th:$PC_{70}BM$ (70:30:1)-based PM OPD. The inset in (A) illustrates the existence of the band bending and tunneling hole injection process at the organic/cathode interface in OPD operated at a reverse bias. The inset in (B) illustrates the presence of the band bending and tunneling hole injection process at the anode/organic interface in OPD operated at a forward bias.

2. *Energy level diagram of dual-mode OPD*

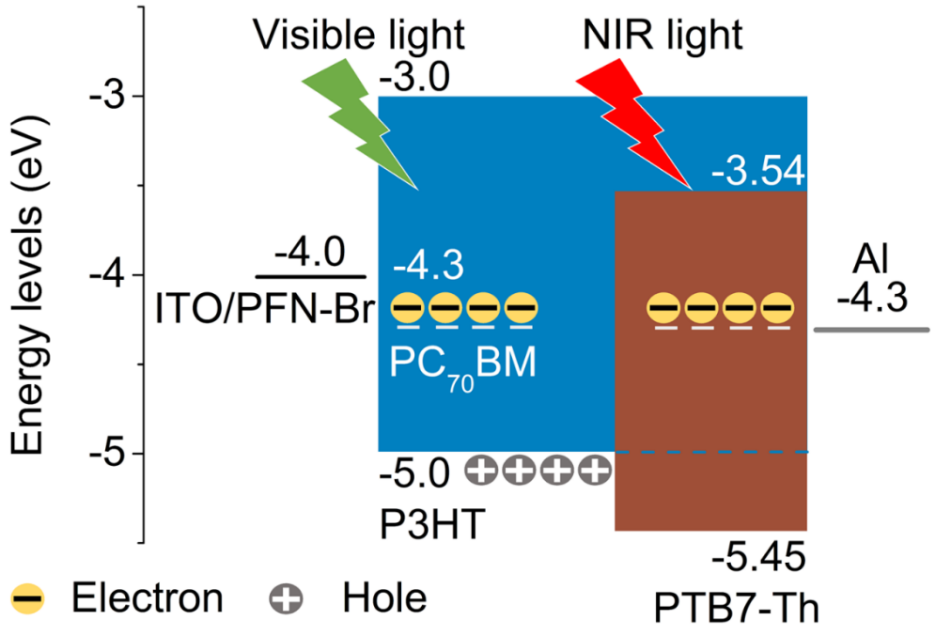

Fig. S2. Schematic energy level diagram of the functional materials used in the dual-mode OPDs.

3. *EQE spectra of the dual-mode OPD*

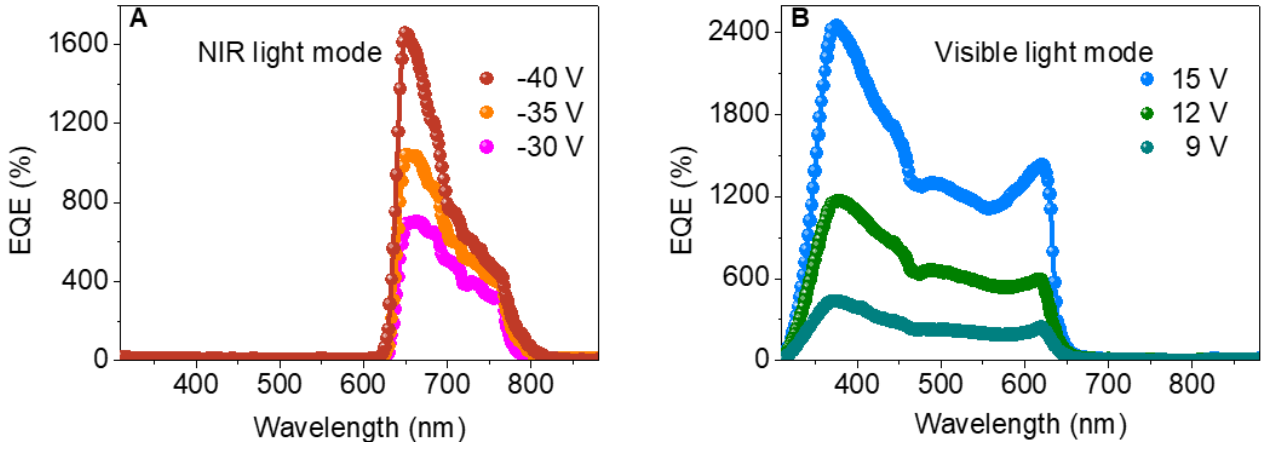

Fig. S3. EQE spectra measured for the trilayer dual-mode OPD at different reverse and forward biases. EQE spectra measured for the tri-layer dual-mode OPD at (**A**) different reverse biases of -30 V, -35 V and -40 V, and (**B**) different forward biases of 9 V, 12 V and 15 V.

4. Dual-mode OPD measurement setup

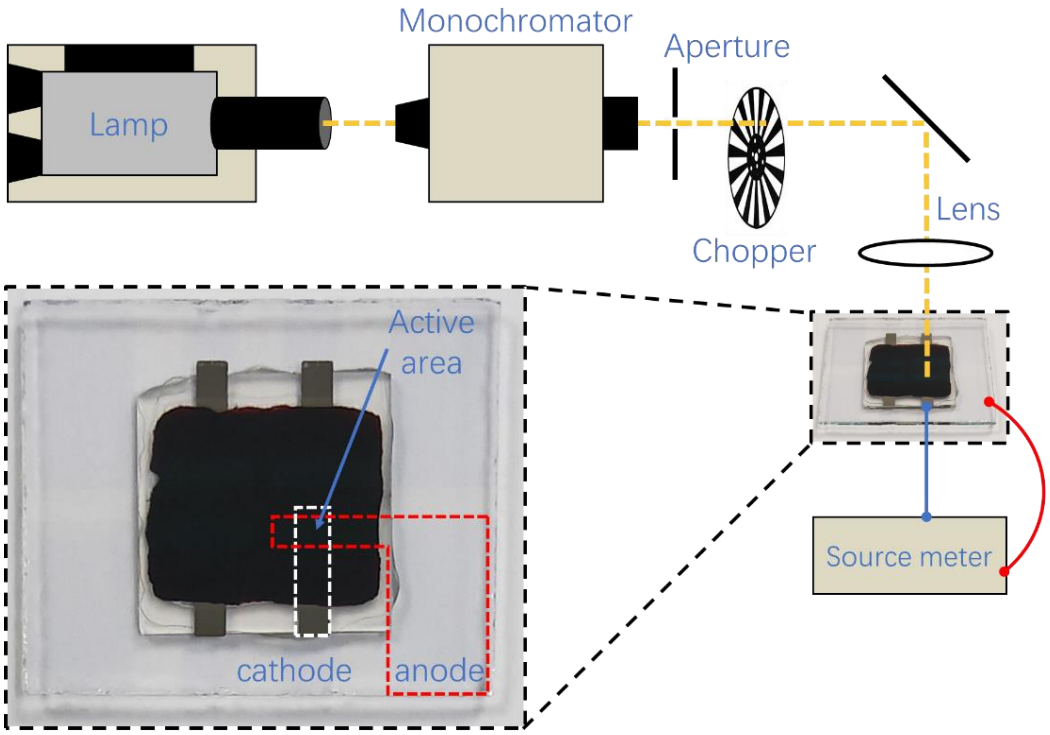

Fig. S4. A schematic diagram illustrating the setup for the measurement of the dual-mode OPD. The photo pictures were taken for the device, showing the layout of the cathode, anode and active region of the dual-mode OPD. (Zhaojue Lan, Hong Kong Baptist University)

5. $J^{0.5}$–V characteristics of hole-only and electron-only devices

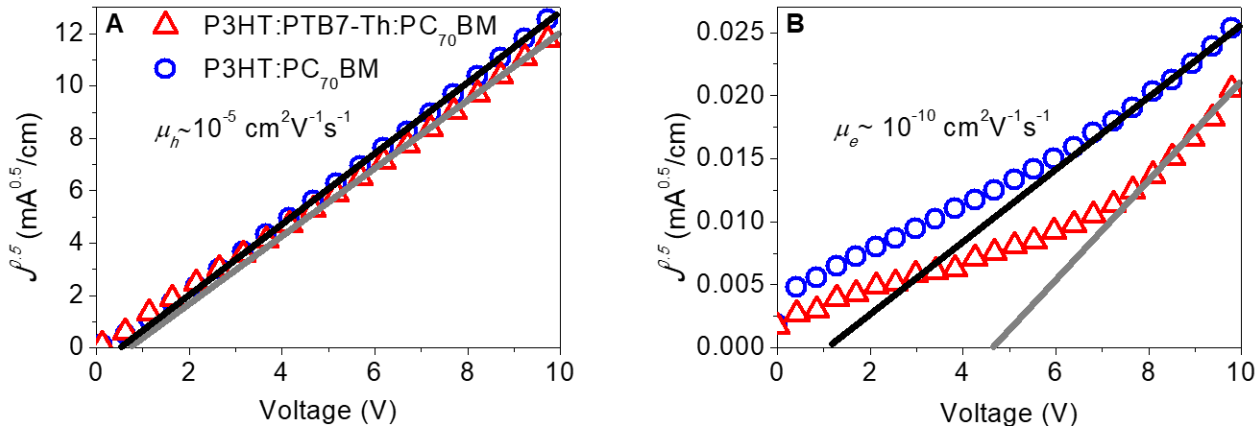

Fig. S5. Charge transport properties of the P3HT:PC_{70}BM (100:1)– and P3HT:PTB7-Th:PC_{70}BM (70:30:1)–based single-carrier devices were analyzed using the space charge–limited current technique. (**A**) $J^{0.5}$–*V* characteristics measured for the hole-only devices: ITO/PEDOT:PSS/P3HT:PC_{70}BM (100:1)/Au (blue circles) and ITO/PEDOT:PSS/P3HT:PTB7-Th:PC_{70}BM (70:30:1)/Au (red triangles). (**B**) $J^{0.5}$–*V* characteristics measured for the electron-only devices: ITO/ZnO/P3HT:PC_{70}BM (100:1)/LiF/Al (blue circles) and ITO/ZnO/P3HT:PTB7-Th:PC_{70}BM (70:30:1)/LiF/Al (red triangles).

6. Optical constants

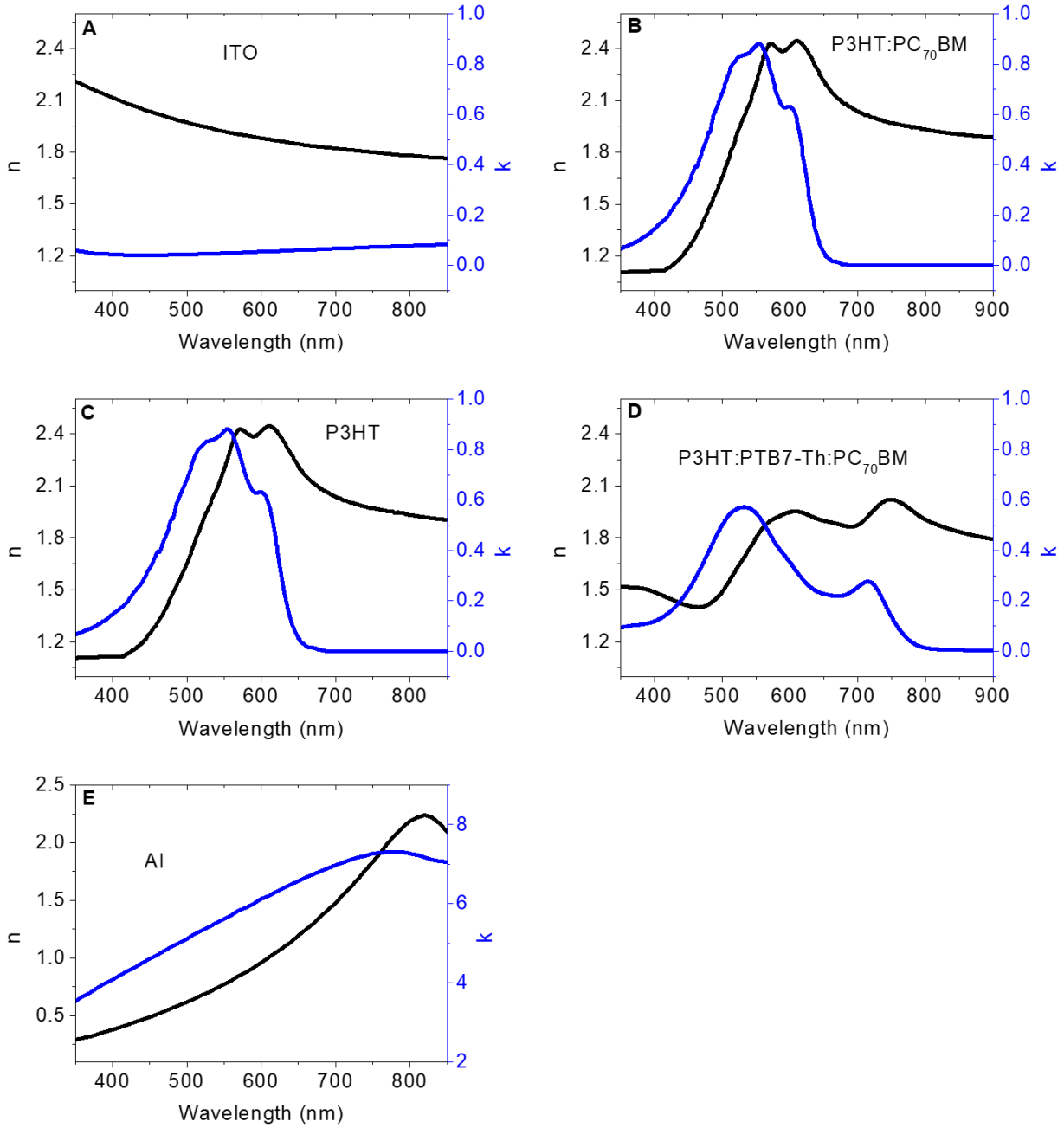

Fig. S6. Optical constants of the functional layers used in the optical simulation in this work. Optical constants, n(λ) and k(λ), measured for the (**A**) ITO, (**B**) binary blend P3HT:$PC_{70}BM$ (100:1), (**C**) pristine P3HT, (**D**) ternary blend P3HT:PTB7-Th:$PC_{70}BM$ (70:30:1) layers, and (**E**) Al used in the optical simulation in this work.

Table S1. Summarized photodetection parameters. The maximum EQE and detectivity measured for the dual-mode OPD using a short wavelength (376 nm) and a long wavelength (654 nm) light sources, operated at different forward and reverse biases.

Light sources	Bias (V)	Dark current ($\times 10^{-7}$A)	Responsivity (A/W)	EQE (%)	D^* ($\times 10^{12}$ Jones)
376 nm	9	0.67	1.31	432	1.79
	12	0.88	3.53	1163	4.20
	15	1.08	7.47	2465	8.03
	18	1.33	14.44	4767	14.01
654 nm	-30	1.07	3.65	692	3.94
	-35	1.33	5.48	1040	5.32
	-40	1.61	8.66	1643	7.64
	-45	2.16	12.94	2454	9.85